Mon. Not. R. Astron. Soc. **000**, 000–000 (0000) Printed 15 November 2007 (MN LATEX style file v2.2)

K-band Imaging of strong Ca II-absorber host galaxies at $z \sim 1$

Paul C. Hewett[1]*, and Vivienne Wild[2]

1. Institute of Astronomy, University of Cambridge, Cambridge CB3 0HA, UK
2. Max-Planck-Institut für Astrophysik, 85748 Garching, Germany

15 November 2007

ABSTRACT

We present K-band imaging of fields around 30 strong Ca II absorption line systems, at $0.7 < z < 1.1$, three of which are confirmed Damped Lyman-α systems. A significant excess of galaxies is found within $6\farcs0$ ($\simeq$50 kpc) from the absorber line-of-sight. The excess galaxies are preferentially luminous compared to the population of field galaxies. A model in which field galaxies possess a luminosity-dependent cross-section for Ca II absorption of the form $(L/L^{*})^{0.7}$ reproduces the observations well. The luminosity-dependent cross-section for the Ca II absorbers appears to be significantly stronger than the established $(L/L^{*})^{0.4}$ dependence for Mg II absorbers. The associated galaxies lie at large physical distances from the Ca II-absorbing gas; we find a mean impact parameter of 24 kpc ($H_0 = 70\,\mathrm{km\,s^{-1}\,Mpc^{-1}}$). Combined with the observed number density of Ca II absorbers the large physical separations result in an inferred filling factor of only $\sim$10 per cent. The physical origin of the strong Ca II absorption remains unclear, possible explanations vary from very extended disks of the luminous galaxies to associated dwarf galaxy neighbours, remnants of outflows from the luminous galaxies, or tidal debris from cannibalism of smaller galaxies.

Key words: dust, extinction - galaxies: ISM, abundances - quasars: absorption lines

1 INTRODUCTION

Quasar absorption line systems are caused by gas clouds lying along the line-of-sight between a background quasar and the observer. Visible through the absorption of the background quasar light the systems provide a unique view of the chemical composition of the gaseous component of the Universe over an extended redshift range. The strongest of the absorption systems probe the densest gaseous regions associated with galaxies; possibly their enveloping gaseous haloes, extended disks or gaseous outflows from winds. Some absorption systems are expected to probe the interstellar medium (ISM) of galaxies, allowing the study of the build up of metals and dust within galaxies out to redshifts comparable to those of the highest redshift quasars. However, the precise link between the absorption– and emission–selected galaxy population is currently unknown.

A key step towards gaining a complete understanding of the nature of quasar absorption line systems is the compilation of a large sample in which the galaxies associated with the absorption have been identified. Such a sample would enable us to link absorption properties with properties of the associated galaxies; luminosity, morphological type and impact parameter for example. A large sample is necessary to understand the effects of factors such as the relative cross–section of different morphological types, metallicity gradients within disks, internal dust content and the effect of outflows on the observed properties of absorption line systems.

Arguably one of the most interesting class of absorption line system for studying galaxies and their immediate environments is damped Lyman-α (DLA) systems, the absorbers with the highest neutral hydrogen column densities. Unfortunately, at $z \lesssim 1$, where deep imaging allows the identification of galaxies several magnitudes below L^{*}, the Lyman-α line moves out of the observed frame optical range and therefore the sample size of known DLAs over more than half the age of the Universe is small. While their low metallicities have led to the suggestion that the host galaxies of DLAs may be low luminosity dwarf galaxies, the small numbers of images obtained thus far have not established any significant difference between the host galaxies of DLAs and the field galaxy population (Chen & Lanzetta 2003; Wolfe, Gawiser, & Prochaska 2005).

Recently Wild & Hewett (2005b) showed that samples of the rare Ca II $\lambda\lambda 3935, 3968$ quasar absorption line systems could be compiled out to cosmologically interesting redshifts, $z \simeq 1$, from quasar spectra in the Sloan Digital Sky Survey (SDSS). Ca II is underabundant in the ISM of the Milky Way due to both its ionisation level – most calcium in the ISM of galaxies is found as Ca III – and its affinity for dust grains. Strong Ca II absorbers at $0.8 \lesssim z_{\mathrm{abs}} \lesssim 1.3$ cause significant reddening of the background

* phewett@ast.cam.ac.uk

quasar light by dust, unlike DLAs and Mg II–selected absorption line systems (Murphy & Liske 2004; Wild, Hewett, & Pettini 2006; York et al. 2006), and an intriguing trend of increasing dust content with increasing Ca II rest–frame equivalent width (W) is observed. Within the Milky Way, Hunter et al. (2006) suggest that Ca II traces warm neutral gas clouds, thus strong Ca II lines at $z \sim 1$ may probe the inner disks of chemically evolved galaxies. Alternatively, large Ca II abundances may arise when dust grains are destroyed, perhaps within shocks caused by major mergers (Wang et al. 2005). The physics of dust is not well understood and destruction of a small fraction of the grains could lead to a large relative increase in gaseous Ca II , consistent with the observed presence of dust in the Ca II systems. A first step towards understanding the true nature of the Ca II systems is through imaging, which, for systems with redshifts below about unity, is well within the capabilities of 4m-class telescopes.

Aside from the objective of understanding the origins of the unusually strong Ca II lines, Ca II absorbers are expected to contain large neutral hydrogen columns, with a significant number above the nominal DLA limit (Wild, Hewett, & Pettini 2006). With $\simeq$400 strong Ca II absorbers in the SDSS Data Release 4 (DR4) quasar sample, compared to the ~ 40 known DLAs at $z \lesssim 1.65$ (Rao, Turnshek, & Nestor 2006), they potentially represent an important new method for the selection of galaxies by hydrogen cross section at low and intermediate redshifts where the Lyman-α line is currently observationally inaccessible.

In this paper we present the results of K-band imaging of the fields around 30 Ca II absorbers with $0.7 < z < 1.2$. The typical number density of K-band objects is well known and low enough for single band imaging to be effective given the expected small impact parameters between the absorbing galaxy and quasar.

The sample selection is described in Section 2 and observations and data reduction in Section 3. In Section 4 we compare our K-band number counts to previous surveys and discuss the impact of potential contamination from the targetting of quasar fields (quasar host and companion galaxies). Section 5 presents our results for the luminosity, impact parameters and morphology of the Ca II absorber galaxies. In Section 6 we first discuss these results in comparison to strong Mg II absorbers and DLAs, then we consider the implications for the present day star formation rate derived in Wild, Hewett, & Pettini (2007). Finally, in Section 7, we discuss viable models for the true nature of Ca II absorption line systems.

Optical apparent and absolute magnitudes taken from the SDSS catalogues are left in the AB-system, while the observed K-band magnitudes are given on the Vega system, as employed by 2MASS. Conversion between the systems can be achieved using the relations $i(\mathrm{AB}) = i(\mathrm{Vega}) + 0.37$, $K_{2\mathrm{MASS}}(\mathrm{AB}) = K_{2\mathrm{MASS}}(\mathrm{Vega}) + 1.86$ and, similarly, for the Mauna Kea Observatory K-band, $K_{\mathrm{MKO}}(\mathrm{AB}) = K_{\mathrm{MKO}}(\mathrm{Vega}) + 1.90$ (Hewett et al. 2006, with m_V=+0.03 for Vega). We use a flat cosmology with $\Omega_\Lambda = 0.7$, $\Omega_M = 0.3$, $H_0 = 100\,h\,\mathrm{km\,s^{-1}\,Mpc^{-1}}$ and $h = 0.7$ throughout the paper.

2 SAMPLE SELECTION

The absorber sample of 30 objects to be imaged was selected from the catalogue of 345 Ca II absorbers described in Wild, Hewett, & Pettini (2007). The absorber redshift range $0.8 \lesssim z_{abs} \lesssim 1.1$ was chosen to probe the old stellar populations associated with absorbers at a significant lookback-time. Three absorbers in the catalogue with N(H I) measurements from Rao, Turnshek, & Nestor (2006) were preferentially targeted, including two with $0.7 < z_{abs} < 0.8$. To avoid complications resulting from the detection of galaxies associated with the background quasar, targets with $z_{quasar} \gtrsim z_{abs} + 0.2$ were selected, with the majority of targets possessing differences of $\Delta z > 0.5$. Otherwise, the make up of the imaging sample was determined by observing constraints, including accessibility of the fields from the United Kingdom Infra-Red Telescope (UKIRT) and the availability of a suitable guide star. The sample includes the full range of quasar brightness and Ca II equivalent width within the catalogue of 345 absorbers.

To summarise, the 30 Ca II absorbers were selected according to the following criteria:

- $0.8 < z_{abs} < 1.2$, *or*, $0.7 < z_{abs} \leqslant 0.8$ with N(H I) from (Rao, Turnshek, & Nestor 2006)
- $z_{quasar} > z_{abs} + 0.2$
- $7^h30^m < \alpha < 18^h00^m$ and $-1^\circ < \delta < 58^\circ$
- Suitable guide star available

In addition, a small sample of five ‘control’ quasars were imaged. The quasars were selected from (Schneider et al. 2005) to have $z_{quasar} \simeq 1.5$, $m_i \simeq 18.0$ and to possess no detected absorption systems with $z_{abs} < 1.2$. Finally, a single ‘blank field’ was also imaged. Table 1 includes the observing log for the target and control sample, along with the positions and redshifts of the targets.

3 OBSERVATIONS AND DATA REDUCTION

The key aim of our observation and data reduction strategy was to obtain a well characterised point spread function (PSF) to allow accurate subtraction of the quasar image and recover candidate absorber host galaxies as faint and close to the quasar as possible.

3.1 Observations

Imaging was undertaken on the 3.8m UKIRT using the Fast-Track Imager (UFTI) near-infared imager (Roche et al. 2003) and a Mauna Kea Observatory K-band filter, over the nights of 2006 April 11 and 14-17 UT. The transparency on 2006 April 11 was variable, but otherwise transparency was good and conditions photometric for a significant fraction of the observations. The median on-chip seeing was $0\farcs62$ full width at half maximum (FWHM), with a full range of $0\farcs40$–$0\farcs85$ FWHM, which was well sampled by the UFTI image scale of $0\farcs091$ per pixel. The on-chip seeing generally improved over the first few hours of observation each night.

An isolated $K_{2\mathrm{MASS}} \simeq 12.3$ star was observed before and after each target to provide a reference PSF for use in the subsequent quasar-subtractions. The default observing sequence for a target consisted of a single 9-point dither of the PSF-star with 5 s exposures, followed by a series of seven 9-point dithers for the target with 40 s exposures, finally, the single 9-point dither of the PSF-star was repeated. The dither offset distance employed was $20''$–$22''$ for both PSF-star and target observations (the small variation from step-to-step was designed to avoid the repeated use of identical columns on the detector). The sequence thus resulted in two 90 s exposures of the PSF-star and a single 2520 s exposure for the target. For a small number of targets, the number of 9-point dithers was varied in order to accommodate observing constraints.

Table 1. Journal of Observations

Name	z_{abs}	z_{quasar}	$m_{i,quasar}$	$m_{K,quasar}$	Exposure (s)	Seeing (")	μ_K [a] (mag arcsec^{-2})	PSF [b]	Observing Date UT
SDSS J074804.06+434138.5	0.898	1.836	18.44	16.7	2520	0.64	21.1	F	2006-Apr-17
SDSS J080735.97+304743.8	0.969	1.255	18.53	16.4	1800	0.84	20.9	F	2006-Apr-11
SDSS J081930.35+480825.8	0.903	1.994	17.64	16.5	2520	0.64	21.2	L	2006-Apr-16
SDSS J083819.85+073915.1	1.133	1.568	18.46	16.7	2520	0.62	21.2	F	2006-Apr-15
SDSS J085221.25+563957.6	0.844	1.449	18.58	16.2	2520	0.56	21.0	F	2006-Apr-16
SDSS J085556.63+383232.7	0.852	2.065	17.57	15.5	2520	0.73	21.2	F	2006-Apr-14
SDSS J093738.04+562838.8	0.978	1.798	18.49	16.2	2520	0.69	21.1	F	2006-Apr-14
SDSS J095307.05+111140.8	0.980	1.877	18.79	16.6	2520	0.75	21.1	L	2006-Apr-15
SDSS J095352.69+080103.6	1.023	1.720	17.40	15.6	2520	0.66	21.1	F	2006-Apr-14
SDSS J100339.44+101936.8	0.816	1.844	18.36	16.7	2520	0.66	21.1	F	2006-Apr-17
SDSS J105930.50+120532.8	1.050	1.570	18.84	16.5	2520	0.53	21.1	L	2006-Apr-15
SDSS J110729.03+004811.2	0.740	1.391	17.10	15.2	2520	0.47	21.1	F	2006-Apr-16
SDSS J113357.55+510844.9	1.029	1.576	18.28	16.7	2520	0.82	21.2	F	2006-Apr-14
SDSS J115523.97+480141.6	1.114	1.542	18.82	16.7	2520	0.51	21.1	L	2006-Apr-16
SDSS J120300.96+063440.8	0.862	2.182	18.47	15.6	2520	0.71	21.2	L	2006-Apr-14
SDSS J122144.62-001141.8	0.929	1.750	18.52	16.9	2520	0.73	21.1	F	2006-Apr-14
SDSS J122756.35+425632.4	1.045	1.310	17.17	15.4	2520	0.56	21.2	F	2006-Apr-15
SDSS J124659.81+030307.6	0.939	1.178	18.81	16.6	2520	0.64	21.2	F	2006-Apr-11
SDSS J130841.19+133130.5	0.951	1.954	18.60	16.6	2520	0.60	21.2	F	2006-Apr-11
SDSS J132323.78-002155.2	0.716	1.388	17.61	15.4	2520	0.64	21.2	L	2006-Apr-17
SDSS J132346.05-001819.8	1.087	1.842	18.84	16.4	2520	0.46	21.1	F	2006-Apr-16
SDSS J140444.19+551636.9	1.070	1.589	18.46	16.5	2520	0.62	21.1	F	2006-Apr-14
SDSS J145633.08+544831.6	0.879	1.518	17.94	16.3	2520	0.56	21.1	L	2006-Apr-11
SDSS J151247.48+573843.4	1.044	2.135	18.69	15.7	2520	0.62	21.1	L	2006-Apr-11
SDSS J153503.36+311832.4	0.904	1.510	17.79	15.8	2520	0.62	21.1	L	2006-Apr-14
SDSS J155529.40+493154.9	0.893	1.831	17.64	15.6	2520	0.51	21.1	L	2006-Apr-14
SDSS J160932.95+462613.3	0.966	2.361	18.67	16.6	3240	0.56	21.2	L	2006-Apr-11
SDSS J164350.94+253208.8	0.885	1.560	17.70	16.0	2520	0.47	21.0	F	2006-Apr-17
SDSS J172739.01+530229.2	0.945	1.442	17.97	16.1	2520	0.47	21.0	F	2006-Apr-16
SDSS J173559.95+573105.9	0.872	1.824	18.18	16.5	2160	0.51	20.9	F	2006-Apr-17
SDSS J093411.14+000519.7	—	1.534	18.08	16.5	2520	0.66	21.0	F	2006-Apr-17
SDSS J114445.93+055053.8	—	1.596	18.02	16.5	2520	0.69	21.1	L	2006-Apr-17
SDSS J142519.70+012043.2	—	1.599	18.09	15.9	2520	0.42	21.1	F	2006-Apr-16
SDSS J150306.34+011345.8	—	1.521	18.09	16.0	2520	0.53	21.1	F	2006-Apr-17
SDSS J160108.43+422937.5	—	1.531	18.05	16.2	2520	0.51	21.1	F	2006-Apr-17
BLANK J132224.4-002155	—	—	—	—	1360	0.62	20.9	—	2006-Apr-16

[a] The surface brightness threshold used to define the galaxy catalogue in the K-band image (Section 3.4)

[b] The source of the PSF-template employed during subtraction of the quasar PSF. F: the template PSF was created from a bright star(s) within the frame; L: the template PSF was selected from a library of PSFs created from specially targetted stars or stars in other quasar frames.

Table 1 presents the journal of observations and includes the exposure time (Col. 5) and on-chip seeing (Col. 6) obtained for each target. Appropriate dark frames were obtained for each PSF-target-PSF sequence.

Photometric zero-points for the target images were obtained by adopting $K_{\rm MKO} = K_{\rm 2MASS}$ for the PSF-stars and applying the zero-points so determined to the target frames. The two PSF-star derived zeropoints for each target were consistent to better than 0.05 mag for all but the observations made on 2006 April 11. The zero-points for the first night indicated attenuation by cloud of 0.1-0.3 mag for several of the observations, but, conditions were changing only slowly and the consistency between pre- and post-target PSF-observations was at worst 0.09 mag. The accuracy of the magnitude zero-points for the target observations are thus $\lesssim$0.05 mag.

3.2 Data reduction

Data reduction techniques employed standard routines available in IRAF[1] The frames were first dark-subtracted using the appropriate calibration frames.

Flatfielding of each PSF-star and target dither was performed using a three-stage procedure. First, a crude flatfield was generated using a 1.75σ-clipped average of all the PSF-star and target frames taken on a given night. The resulting nightly flatfields were normalised and divided into the individual frames. The OBJMASKS routine was then used to exclude areas of the frames affected by astronomical objects and the generation of the nightly average flatfield repeated. Division of the individual frames by these improved

[1] IRAF is distributed by the National Optical Astronomy Observatories, which are operated by the Association of Universities for Research in Astronomy, Inc. under cooperative agreement with the National Science Foundation.

flatfields produced good results for both PSF-star and target frames, but low-level structure in the sky was still visible at the 1 per cent level. The final step in the flatfielding involved rerunning the OBJMASKS routine on the flatfielded frames and then generating a 2σ-clipped average of the 9 (63) frames in each PSF-star (target) sequence. Division of each frame by the resulting final flatfield reduced the structure in the sky to $\lesssim 0.3$ per cent.

The master PSF-star (target) image was generated from a 5σ-clipped average of the 9 (63) frames, employing the appropriate XY-offsets for the dither pattern. A bad-pixel mask, derived from the dark frames and the variance of the nightly flatfield frames, was employed to exclude bad pixels from the averaging. The resulting frames were both cosmetically clean and showed no detectable structure in the sky. The combined image was then clipped to retain just the central fully-exposed 536×536 pixel ($49'' \times 49''$) region.

3.3 Point spread function subtraction

In order to identify faint galaxies with small projected separations from the quasars, subtraction of the quasar images was undertaken using the standard sequence of DAOPHOT routines (Stetson 1987) in IRAF. A 21 pixel ($1\farcs9$) radius aperture was used to define the PSFs and also for the quasar image subtractions. The PSF-star images were analysed using the PSF routine to produce a library of template-PSFs. All the PSF-star images were best-fit by a Moffat profile, usually with $\beta = 1.5$, although the images obtained in the poorest seeing typically produced a best-fit with $\beta = 2.5$.

The target frames were then inspected visually and additional template-PSFs were constructed using the DAOPHOT routines, where a single stellar image brighter than $m_{quasar} + 0.5$ was present in the frame. The number of target frames for which two or more such suitable stars were present was small but in such cases a single template-PSF was constructed. Care was taken to ensure that none of the stellar images possessed peak counts taking them into the non-linear exposure–count regime of UFTI.

The subtraction of the quasar images was undertaken using the SUBSTAR routine. As expected, the template-PSFs derived from a particular target frame produced the most satisfactory subtractions for the target quasar. Where such a template-PSF was not available, a suitable template-PSF was chosen from the full library based on the seeing, ellipticity and orientations of fainter stellar images in the target frame. Table 1, Col. 9 indicates whether the adopted PSF-subtraction employed a library (L) or target frame (F) PSF.

The results of all the subtractions were examined visually and a series of tests carried out to verify the reliability of the quasar-image removal. In cases where a faint image was revealed by the subtraction, other stellar images (when present) in the target frame were also processed to ensure that similar 'images' were not revealed. Similarly, when low-level systematic residuals, usually of the 'butterfly' or 'clover-leaf' type, were present[2], other stellar images were processed to ascertain that the same form of residual persisted. In all cases, irrespective of whether faint images or residuals were apparent, a number of different PSF-templates were tested to check that the results of the image subtraction was not strongly dependent on the exact PSF-template used. Fig. 1 shows the pre- and best post-subtracted quasar images for the 30 Ca II quasars and the five control quasars. Each image pair shows a $15\farcs0 \times 15\farcs0$ region centred on the quasar, with the pre-subtraction image presented on the right-hand side. A scale-bar is shown in the top right-hand panel of each page.

The combination of the UFTI instrument, with its small $0\farcs091$ pixels, and an observing strategy in which high signal-to-noise ratio target and PSF-star observations were obtained was designed to maximise the accuracy of the PSF characterisation. The resulting image subtractions were well-behaved with the form of the residuals showing consistent behaviour among multiple stars within the same frame, and as a function of the degree of similarity between the PSF-templates and the image profiles. However, the magnitude range of the quasars, $15.4 \leqslant K \leqslant 16.9$, causes a significant variation to exist in the magnitude of the faintest galaxies that may be detected reliably, as the PSF-subtraction is limited in accuracy by a constant percentage of the quasar flux.

To determine the effectiveness of the PSF-subtraction a series of simulations were undertaken using the ARTDATA package within IRAF. Synthetic galaxies, modelled pessimistically as pure exponential disks, were blurred to match the seeing using a Moffat profile. To match the appearance of galaxies in the images, these synthetic galaxies were constructed with intrinsic half-light radii of $0\farcs1$ to $0\farcs25$, corresponding to spatial half-light diameters of $\sim$2-5 kpc, and a range of apparent magnitude $19.0 \leqslant K \leqslant 20.0$. The synthetic galaxies were then added to the actual frames of absorber and control quasars that were not found to possess close companion galaxies. Three quasar-galaxy separations of $\Delta\theta = 0\farcs0, 0\farcs5$ and $1\farcs0$ were explored, using quasar images covering the full magnitude range of quasars present in the sample.

The results of the simulations were encouraging. At separations $\Delta\theta \geqslant 1\farcs0$ the galaxy images are visible in the pre-PSF-subtracted images for all but the brightest quasars, and all galaxies as faint as $K = 20.0$ are recovered. Down to separations of $\Delta\theta \geqslant 0\farcs5$ all galaxies with $K = 19.5$ are revealed via the PSF-subtraction. Fainter than $K = 19.5$, galaxies can be detected down to $K = 20.0$ only for the faintest third of the quasar images ($K \geqslant 16.5$). The recovery rate for essentially zero-separations, $\Delta\theta \lesssim 0\farcs25$, is poor. Galaxies with $K \geqslant 19.5$ cannot be recovered for any of the quasars and galaxies with $19.0 \leqslant K < 19.5$ can only be recovered for quasars with $K \geqslant 16.0$. The rapid degredation in the ability to recover faint galaxies at the very smallest separations comes about primarily because of the presence of the characteristic 'butterfly' or 'clover-leaf' residuals, which are caused by very small differences in the PSFs and potential confusion from the cores of quasar host galaxies. In summary, the PSF-subtraction is capable of recovering galaxies with percentage fluxes of the quasar of 1, 1.5 and 7 per cent at separations of $\Delta\theta = 1\farcs0, 0\farcs5$, and $0\farcs0$ respectively. Notes regarding the results of the PSF-subtraction for a small number of quasars are included in Appendix 7.

3.4 Object catalogue generation

The high-resolution of the raw images, necessary for the image subtractions, was not optimal for the detection of faint low-surface brightness images within the target exposures. Image catalogues, including the detection of the target quasar or quasar+close_companion, were constructed by applying SEXTRACTOR (Bertin & Arnouts 1996) to the pre- and post-PSF-subtracted images, rebinned by a factor of two to produce $0\farcs182$ pixels. A 1σ threshold above the sky level, equivalent to a surface-brightness threshold $\mu_K \simeq 21.1$ mag arcsec^{-2}, was employed with a Gaussian detection kernel matched to the seeing of the target frame. Cols. 6 and 7 of Table 1 list the seeing and surface-

[2] see the subtracted images of J120300.96+063440.8 and J155529.40+493154.9 respectively, in Fig. 1 for clear examples of the residual morphologies

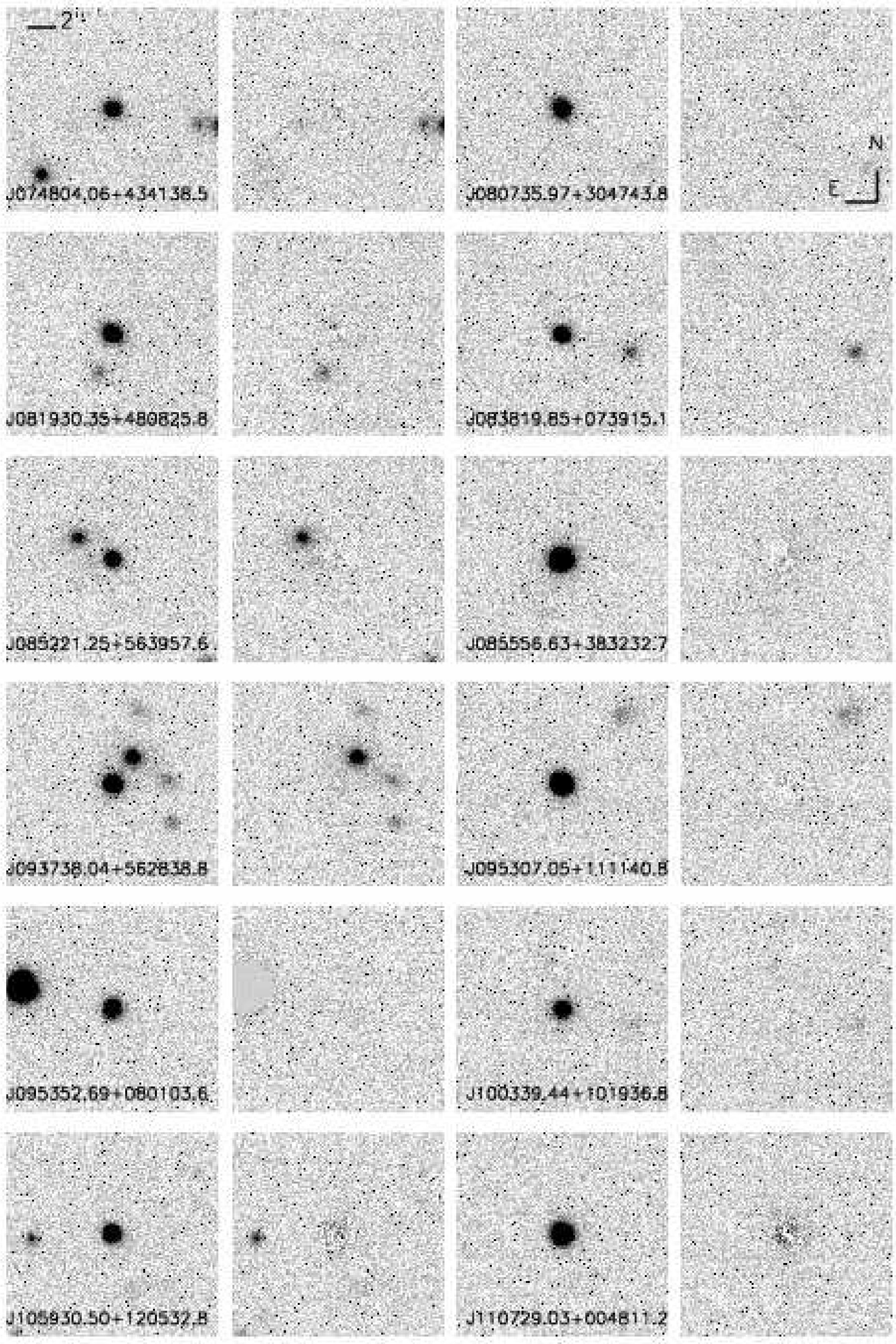

Figure 1. Images of the 30 Ca II -absorber quasars and the five control quasars. The left-hand panel in each pair shows the K-band image of the quasar field, while the right-hand panel shows the quasar field after subtraction of the quasar. Each images is $15.''$ on a side. A scale-bar is shown in the image at top left on each page and the orientation of the images is indicated in the image at top right on each page.

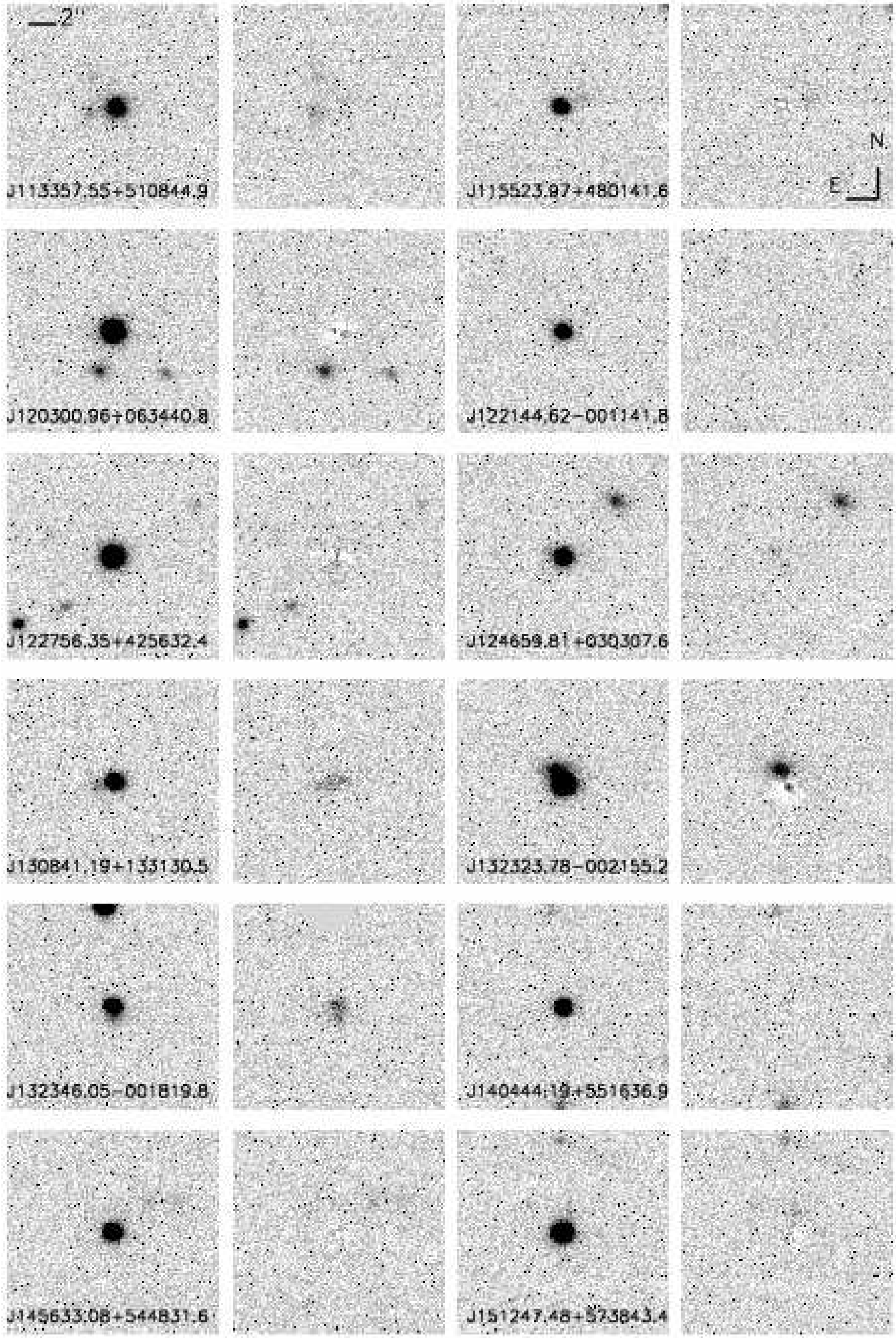

Figure 1 (continued)

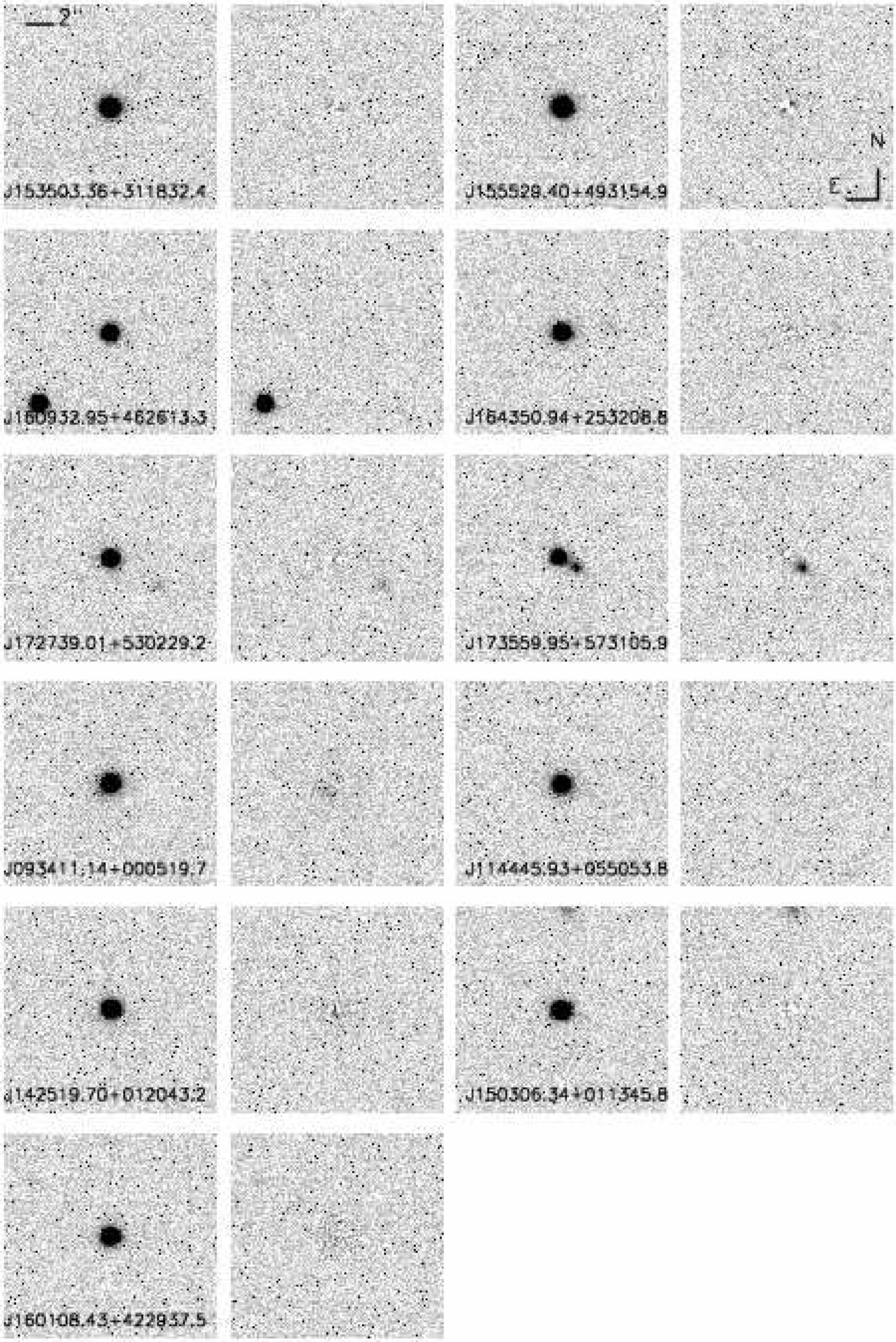

Figure 1 (continued)

brightness thresholds for each target frame. Visual inspection of the target frames confirmed the effectiveness of the SEXTRACTOR analysis and the resultant objects catalogues were not sensitive to small changes in the detection parameters.

All the detected objects in the frames were inspected visually and a small number ($\simeq$10) at the extreme edges of the frames, or resulting from a faint satellite trail in one target frame, were eliminated. The number of objects detected in each target frame (typically $\simeq$10) was too small for the morphological image classification provided by SEXTRACTOR to prove reliable. Consequently, all objects with $K \leqslant$18.5 were classified visually. PSF-fitting was employed in the few cases where any doubt concerning the classification arose.

The SEXTRACTOR MAG_BEST parameter was used to provide the magnitude estimate for the detected objects. The magnitudes of the quasars were taken from the values provided by the DAOPHOT SUBSTAR routine. After applying the zero-points for each target frame (Section 3.1) we detect $K = 20.0$ objects in all frames, with the catalogues from the longest exposures in the best seeing containing objects as faint as $K = 21.0$. Magnitude errors are estimated from the detected electrons per object and an additional approximation, to take account of the uncertainty in the sky-background determination, calculated by shifting the sky-level under the total area of the image by 20 per cent of the 1σ pixel-to-pixel fluctuations in the sky background.

Table 2 presents the catalogue of nearest neighbour galaxies, including *all* galaxies within 6.″0 of each quasar. Cols. 2, 3, and 4 give the quasar-galaxy separations in arcseconds and Col. 5 gives the galaxy K-band magnitude. The final column specifies whether the galaxy is the first-, second-, third- or fourth-nearest neighbour to the quasar.

4 THE K-BAND IMAGES OF THE ABSORBER SIGHT-LINES

4.1 K-band number counts

The total sky coverage of the 36 fields, each covering a $47.''8 \times 47.''8$ region, excluding a 1.″0 strip at the frame edges where the image catalogues will be incomplete, is 22.8 arcmin^2. Excluding a 6.″0 radius circle centred on each of the 35 quasars, which will be used in subsequent analysis of galaxies associated with the quasar absorber, reduces the area to 21.7 arcmin^2. The number of galaxies is relatively small but the number-counts (Table 3) are consistent with the results of the K20 survey and the compendium of K-band imaging results presented by Cimatti et al. (2002). The contribution of stars to the counts fainter than $K = 18.5$ at the high Galactic latitudes of the fields is expected to be small ($\lesssim 5$ per cent) (Cimatti et al. 2002) and all objects fainter than $K = 18.5$ are treated as 'galaxies' in subsequent statistical analysis. The large number of widely-separated fields reduces the impact of large scale structure on the number-counts but, nonetheless, the Poisson errors associated with the observed numbers of galaxies underestimate the uncertainties given the clustering of galaxies.

4.2 Galaxies at the quasar redshifts

The selection of the absorber sample deliberately included a bias towards quasars with redshifts well above those of the absorbers. A small sample of quasars without known intervening absorption line systems was also imaged to provide an empirical control sample. The median redshift of the quasar sample is z_{median}=1.65 and only five quasars possess redshifts $z < 1.4$.

There are three independent results which consistently indicate a low level of contamination of the number–magnitude counts by galaxies physically associated with the quasars themselves. Firstly, the spectroscopic results from the K20 survey show only 9 per cent of their $K \leqslant 20.0$ sample to possess redshifts $z > 1.5$ Cimatti et al. (2002). Secondly, the small control sample of five quasars with $z \simeq 1.5$ contains just a single galaxy detected within a radius of 6.″0. Finally, the number of galaxies detected within 6.″0 of the absorber sample quasars as a function of quasar redshift also provides no evidence for significant contamination: 16 galaxies were detected around the 15 quasars with $z < z_{median}$, with 14 galaxies detected around the 15 quasars with $z > z_{median}$; and of the five quasars with $z < 1.4$, two have no detected galaxies.

Table 3. Integral number-magnitude counts for the 'field' compared to the predictions from the K20 survey (Cimatti et al. 2002).

Magnitude	N_{obs}	N_{K20}
$K \leqslant 18.0$	28±5	44±5
$K \leqslant 19.0$	96±10	122±8
$K \leqslant 20.0$	221±15	204±9

4.3 Quasar host galaxies

The K-band magnitudes of host galaxies of quasars with $1 \leqslant z \leqslant 2$, which are not strong radio sources and possess absolute magnitudes within the range covered by our sample, are typically $K \sim 19$ (e.g. Falomo et al. 2004; Kotilainen et al. 2006). While no account of the radio properties of the quasars was taken when selecting the sample, only one of the quasars (SDSS J120300.96+063440.8 at z=2.182, with a ratio of radio to i-band optical flux $R_i \simeq 3.3$) is a strong radio source ($R_i > 1.0$ Ivezić et al. 2002).

Although the expected magnitudes of the quasar host galaxies lie above the magnitude limit of our object catalogues ($K = 20.0$), the size and surface brightness properties of the host galaxies effectively preclude their detection via the techniques employed to identify potential absorber host galaxies. The quasar host galaxies are physically large, with half-light radii typically exceeding 1.″0, and the surface brightnesses are low, not least because of the rapidly increasing impact of the $(1 + z)^4$ cosmological dimming as z_{quasar} exceeds unity. The K-band observations of Falomo et al. (2004) and others involve exposure times equivalent to a factor ∼4 larger than those presented here and peak surface brightnesses of the detected host galaxies are typically found to be $\mu_K \gtrsim 20$ mag arcsec^{-2} for quasars that are not strong radio sources.

The almost complete lack of extended, approximately symmetric sources surrounding the quasar images is thus not surprising given the much higher surface brightness thresholds, $\mu_K \simeq 21.1$ mag arcsec^{-2}, to which our imaging reaches. It is certainly possible that a number of small, faint, $K > 20.0$, residuals centred on the PSF-subtracted quasar images could be the higher surface brightness cores of host galaxies but the presence of any such hosts does not result in contamination of the catalogue of $K \leqslant 20.0$ objects that forms the basis for the statistical analysis of the absorber hosts.

Table 2. All companion galaxies within 6.″0 from the absorber, or the nearest neighbour if no closer galaxies are seen. Col 2–4: angular offsets from the background quasar, Col 5: apparent magnitudes, Col 6: first, second, third or fourth nearest neighbour, Col 7-8: probability of being a field galaxy, Col 9: Absolute magnitude.

Quasar Name	ΔRA (")	ΔDec (")	$\Delta\theta$ (")	K	Neighbour	$P_{\rm Field}(m)^a$	$P_{\rm Field}(\Delta\theta)^b$	$M_K{}^c$
Absorber Quasars								
J074804.06+434138.5	2.7	-1.2	2.9	19.26±0.21	1	0.040	0.267	-23.02
J080735.97+304743.8	-5.8	-4.2	7.2	19.31±0.12	1	—	—	—
J081930.35+480825.8	0.9	-2.8	2.9	18.53±0.18	1	0.291	0.267	-23.76
J083819.85+073915.1	-4.9	-1.3	5.0	18.40±0.14	1	0.323	0.419	-24.43
J085221.25+563957.6	1.7	-0.2	1.7	18.82±0.19	1	0.396	0.133	-23.31
J085221.25+563957.6	2.4	1.5	2.8	17.18±0.14	2	0.182	0.267	-24.94
J085556.63+383232.7	1.1	-3.9	4.0	19.35±0.11	1	0.246	0.480	-22.80
J093738.04+562838.8	-1.4	1.9	2.4	16.80±0.11	1	0.389	0.267	-25.68
J093738.04+562838.8	-3.8	0.3	3.8	18.00±0.18	2	0.107	0.467	-24.48
J093738.04+562838.8	-4.2	-2.8	5.0	18.90±0.19	3	0.793	0.419	-23.58
J093738.04+562838.8	-1.9	5.2	5.6	18.67±0.20	4	0.368	0.419	-23.81
J095307.05+111140.8	-8.0	-3.7	8.8	19.28±0.19	1	—	—	—
J095352.69+080103.6	-4.4	5.1	6.7	18.19±0.16	1	—	—	—
J100339.44+101936.8	-5.0	-1.1	5.1	19.52±0.18	1	0.328	0.419	-22.53
J105930.50+120532.8	-1.6	-4.1	4.4	19.39±0.14	1	0.116	0.480	-23.25
J105930.50+120532.8	5.7	-0.4	5.7	18.60±0.13	2	0.221	0.419	-24.05
J110729.03+004811.2	16.1	6.3	17.3	18.98±0.19	1	—	—	—
J113357.55+510844.9	1.6	-0.3	1.6	18.06±0.12	1	0.170	0.133	-24.53
J115523.97+480141.6	-1.6	0.6	1.7	19.28±0.17	1	0.219	0.133	-23.51
J120300.96+063440.8	0.9	-2.9	3.0	18.16±0.14	1	0.248	0.267	-24.02
J120300.96+063440.8	-3.7	-3.0	4.8	19.26±0.14	2	0.069	0.480	-22.92
J122144.62-001141.8	-2.3	-9.0	9.3	19.28±0.14	1	—	—	—
J122756.35+425632.4	4.3	1.8	4.6	19.95±0.18	1	0.905	0.480	-22.69
J122756.35+425632.4	3.3	-3.7	4.9	19.21±0.17	2	0.839	0.480	-23.42
J124659.81+030307.6	0.8	0.2	0.8	19.24±0.17	1	0.110	0.089	-23.14
J124659.81+030307.6	-3.7	4.1	5.6	17.96±0.15	2	0.066	0.419	-24.42
J130841.19+133130.5	0.5	-0.0	0.5	18.30±0.14	1	0.166	0.089	-24.11
J132323.78-002155.2	0.4	1.0	1.1	17.26±0.13	1	0.416	0.133	-24.48
J132346.05-001819.8	0.0	-0.3	0.3	17.93±0.15	1	0.507	0.089	-24.80
J140444.19+551636.9	0.8	7.0	7.1	19.46±0.18	1	—	—	—
J145633.08+544831.6	-2.6	2.2	3.4	19.42±0.21	1	0.319	0.467	-22.80
J145633.08+544831.6	-4.7	2.3	5.2	19.55±0.16	2	0.223	0.419	-22.67
J151247.48+573843.4	-0.6	1.5	1.6	19.61±0.27	1	1.000	0.133	-23.03
J153503.36+311832.4	-17.2	-3.5	17.6	19.22±0.21	1	—	—	—
J155529.40+493154.9	-18.0	17.8	25.3	17.61±0.15	1	—	—	—
J160932.95+462613.3	-2.9	-11.5	11.8	19.76±0.22	1	—	—	—
J164350.94+253208.8	-3.4	0.4	3.5	19.96±0.23	1	0.237	0.467	-22.28
J172739.01+530229.2	-3.3	-1.8	3.7	19.38±0.19	1	0.124	0.467	-23.02
J173559.95+573105.9	-1.0	-0.6	1.2	18.28±0.15	1	0.177	0.133	-23.93
Control Quasars								
J093411.14+000519.7	-0.6	-0.5	0.8	17.82±0.11	1	—	—	—
J114445.93+055053.8	12.6	0.0	12.6	19.76±0.15	1	—	—	—
J142519.70+012043.2	1.4	9.7	9.8	18.77±0.17	1	—	—	—
J150306.34+011345.8	0.5	7.3	7.3	18.76±0.18	1	—	—	—
J160108.43+422937.5	-8.6	2.7	9.0	18.92±0.19	1	—	—	—

[a] Probability the galaxy is a field galaxy, given its apparent magnitude.
[b] Probability the galaxy is a field galaxy, given its projected distance from the absorber.
[c] Vega magnitudes, $\mathrm{H}_0 = 100\,\mathrm{km\,s^{-1}Mpc^{-1}}$

4.4 The companion galaxy catalogue

The discussion in the preceding sub-sections indicate that the census of galaxies with $K \leqslant 20.0$ is essentially complete to within 1.″0 of the quasar images. Fainter than $K \simeq 19.0$, the census is substantially incomplete for galaxies with very small $\lesssim 0.''5$ separations from the quasar. The corresponding spatial separations are small however, corresponding to scales $\lesssim$4 kpc. The galaxy catalogue is also expected to suffer from little contamination by quasar host galaxies or other galaxies at the quasar redshifts, based both on prior expectations from larger K-band surveys and on the lack of any empirical evidence from the imaging observations themselves. The statistics of the sample of galaxies presented in Table 2 should thus provide direct constraints on any population of galaxies asso-

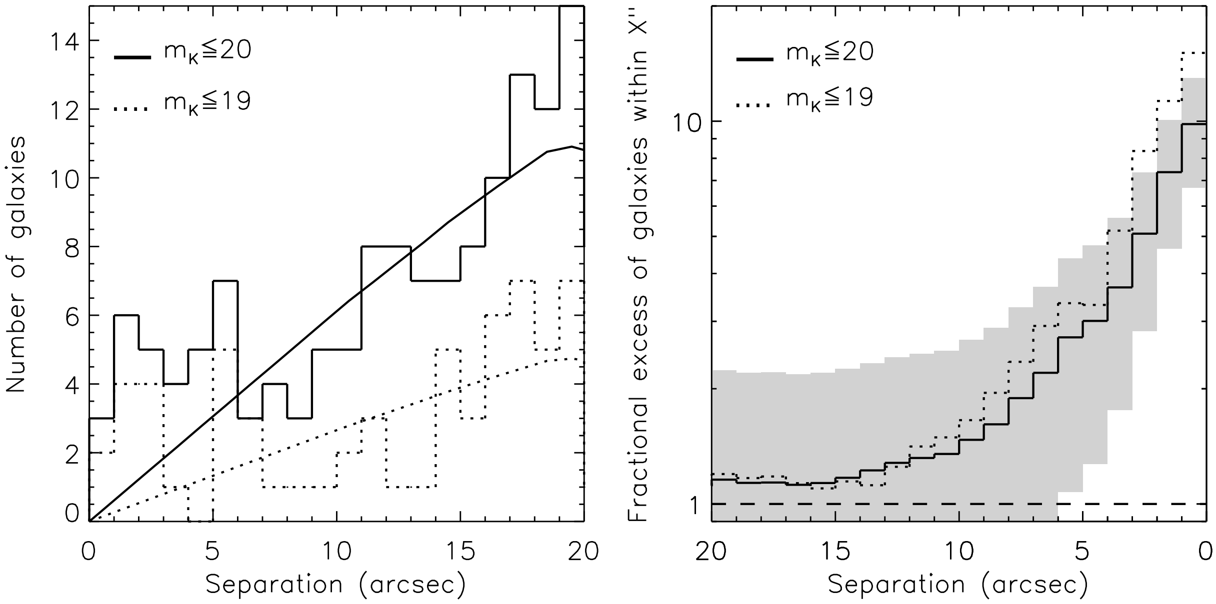

Figure 2. *Left:* Number of galaxies with $K \leqslant 20$ as a function of projected distance from the quasar, in bins of $1.''0$. *Right:* Cumulative number of galaxies with $K \leqslant 20$ (full line), $K \leqslant 19$ (dotted line). In both figures, the histograms are the observations and the continuous lines are the predictions assuming no excess of galaxies around the position of the absorber.

ciated with the Ca II absorbers that are bright enough to be included in the $K \leqslant 20.0$ sample.

The effectiveness of an imaging survey for constraining the presence of associated galaxies depends on: i) the number of targets, ii) the surface density of unrelated galaxies and iii) the number of associated galaxies per target. Figure 2 presents the number counts of galaxies detected in our survey, as a function of separation from the absorber. On the right we show the observed number of galaxies within a given radius, divided by that predicted; the grey shading shows the associated Poissonian errors for the magnitude limit of 20. For our observations, the angular scale on which such an excess population could be identified with any significance is $\simeq$5-7$''$ and we chose a radius of $6.''0$ for the presentation of the associated galaxy statistics. We have not attempted to maximise the significance of the excess by optimising the choice of magnitude limit and separation (e.g. quoting statistics for the excess at $<3.''0$ with a magnitude limit of $K \leqslant 19.0$).

The existence of a galaxy overdensity close to the quasars with intervening Ca II absorbers is clear. Table 5 summarises the number-counts within $6.''0$ for the absorber and control quasars down to magnitude limits of $K = 19.0$ and 20.0. The predicted numbers of galaxies are calculated from the number counts of galaxies at $\Delta\theta > 6.''0$ from the target quasar in all target fields (Section 4.1). The numerical excess of galaxies observed is high, with observed:predicted numbers of 30:9.6 and 16:4.2 for magnitude limits of $K = 20.0$ and 19.0 respectively. Figure 2 illustrates the form of the observed excess as a function of separation. The quasars are widely separated on the sky and large-scale structure is not an issue but the small-scale clustering of galaxies may be expected to enhance the apparent overdensity. However, allowing only *one* galaxy within a $6.''0$ radius of each absorber quasar to contribute to our number count of observed galaxies, gives observed:predicted numbers of 21:9.6 and 12:4.2 for magnitude limits of $K = 20.0$ and 19.0 respectively. The significance of the excess at both magnitudes is $\simeq 3\sigma$. The statistics for the small control sample of quasars are entirely consistent with the predictions from the field K-band number counts.

5 PROPERTIES OF THE ABSORBER-ASSOCIATED GALAXIES

5.1 The galaxy luminosity function

The form of the local K-band galaxy luminosity function (GLF) is now well-established (Table 4 of Kochanek et al. 2001) and we adopt the Schechter fit presented in this paper, with $M^*_K = -23.39$ (for $H_0 = 100\,\mathrm{km\,s^{-1}}$) and $\alpha = -1.09$, as our fiducial reference when considering the absolute magnitude distribution of the galaxies apparently associated with the Ca II absorbers.

The K-band observations probe the rest-frame wavelength region $\sim$10 000 Å ($z = 0.7$) to $\sim$13 000 Å ($z = 1.2$) where the galaxy light is dominated by K-giant stars. As a result, the K-corrections in the K-band are largely insensitive to the spectral type of the galaxies. Galaxies observed at increasing redshift are expected to brighten, as their stellar populations become younger, and there is broad agreement between the predictions of theoretical models (e.g. Pozzetti, Bruzual, & Zamorani 1996) and observations (Drory et al. 2003; Saracco et al. 2006). To characterise the evolution we adopt a simple pure luminosity evolution model for the GLF, with the characteristic absolute magnitude evolving as $M^*_K(z) = M^*_K(z = 0) - 0.53z$, as determined by Drory et al. (2003). Our observations probe a magnitude range typically within ± 1.5 mag of M^*_K and possible variations in the slope of the faint end slope of the GLF do not significantly affect our results. Cols.

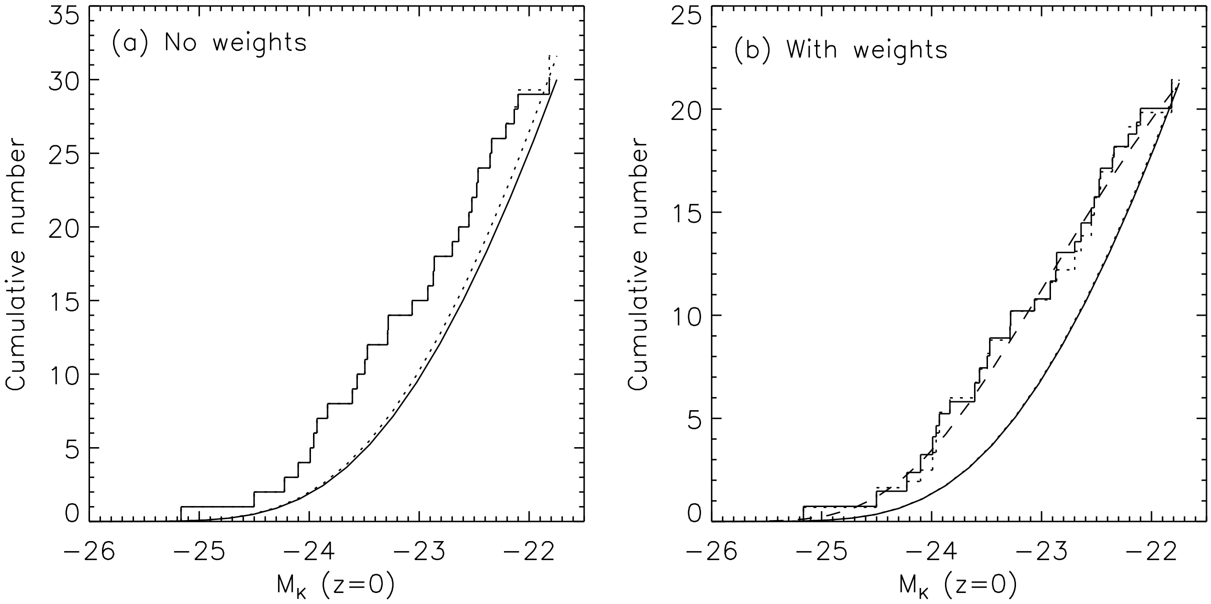

Figure 3. The $z = 0$ cumulative galaxy luminosity function (GLF) of galaxies within 6.″0 from the absorber, assuming they lie at the redshift of the absorber (stepped histograms). *Left:* All galaxies are included, as observed. The dotted histogram accounts for the magnitude limit of the survey. *Right:* Two weighting schemes are applied to allow for interlopers, based on each galaxy's distance from the absorber (full histogram) or each galaxy's apparent magnitude (dotted histogram). The smooth overplotted lines are the $z = 0$ K-band luminosity function of Kochanek et al. (2001). In the right hand panel, the dashed line results from scaling this luminosity function by $L^{0.7}$, our best match to the Ca II –selected galaxies (see text).

2 and 3 of Table 4 presents K-corrections as a function of redshift for galaxies of two spectral types. Absolute magnitudes before and after accounting for redshift evolution are given for objects with $K = 18.0$ and 20.0 in Cols. 4, 5, 7 and 8. Finally, luminosities relative to L^* are provided in Cols. 6 and 9. The K-band at $z{\simeq}1$ approximates the J-band at z=0.0 and the K-corrections and luminosity evolution are well-defined at the relatively long wavelengths probed by the K-band observations. Beginning with the J-band luminosity function of Cole et al. (2001) and using the observed K-band GLF at $z{\simeq}1$ from Pozzetti et al. (2003) results in luminosities for the galaxies, relative to L^*, that are essentially indistinguishable from those calculated above.

A GLF for the galaxies nominally associated with the absorbers can be constructed by calculating the absolute magnitude of each of the galaxies where an excess is observed, assuming they lie at the redshift of the absorber. After correcting for the effects of redshift evolution as described above, a z=0.0 GLF is constructed which may be compared with the local GLF derived by Kochanek et al. (2001). There are two statistical corrections that must first be made before proceeding.

Firstly, although the limiting absolute magnitude, corresponding to the $K = 20.0$ apparent magnitude limit, does not vary enormously over the absorber redshift range, a number of the fainter galaxies detected in the lower redshift absorber fields could not have been detected at the redshifts of all the observed fields. Each galaxy is therefore weighted by the factor $N_{\rm Detect}/N_{\rm Field}$, where $N_{\rm Detect}$ is the number of absorber fields in which a galaxy of given absolute magnitude is detectable and $N_{\rm Field} = 30$ is the total number of fields we observe[3].

Secondly, from the field number density (Section 4.1) we expect 9.6 galaxies of the 30 galaxies detected within a 6.″0 radius of the background quasar not to be associated with the absorber, and we would like to account for these as best we can. In what follows we designate $P_{\rm Field}$ as the probability that the galaxy is *not* associated with the absorber; the average value is $< P_{\rm Field} >= 9.6/30 = 0.32$. We can use our prior knowledge of the number-density and number-magnitude counts of the field galaxies to predict for each of our galaxies a more accurate probability that it is an interloping field galaxy, and then weight the contribution of each galaxy to the GLF by individual $1 - P_{\rm Field}$ factors. While we could combine the priors into a single weighting scheme, we chose to adopt algorithms based on each prior separately, to ensure that the GLF is not sensitive to the precise scheme for the assignment of the probabilities. Combining the weighting schemes gave a consistent result.

The first weighting scheme accounts for the fact that the excess of galaxies around the target quasar is observed to be a function of distance from the quasar. The individual $1 - P_{\rm Field}$ factors then take account of the increasing likelihood that a galaxy closer to the quasar is associated with an absorber than one further away. Galaxies in each annulus ($\Delta\theta$=0.″0–1.″0,1.″0–2.″0,...,5.″0- -6.″0) are assigned a value of:

$$P_{\rm Field} = n_{\rm Field}/n_{Obs} \qquad (1)$$

[3] This correction is directly equivalent to the common $\rm V_{max}$ correction employed in calculating mean properties of galaxies in redshift surveys.

where $n_{\rm Field}$ and n_{Obs} are the predicted and observed number of galaxies within the annulus respectively. The second scheme is based on our prior knowledge of the apparent magnitude distribution of K-band selected galaxies. Adopting the form of the K-band number counts from Cimatti et al. (2002), magnitude limits of K=15.0 and 20.0, and ordering the galaxies, i=1,2,...,30, by increasing magnitude, K, galaxies are assigned a value of:

$$P_{\rm Field,i} \propto n_{\rm Field}(15 \leqslant m \leqslant m_i + 0.5(m_{i+1} - m_i)) \\ -n_{\rm Field}(15 \leqslant m < m_i - 0.5(m_i - m_{i-1})) \quad (2)$$

where $n_{\rm Field,i}$ is the predicted number of galaxies with K-band apparent magnitudes between the limits for galaxy i and the results are normalised such that $< P_{\rm Field} >= 0.32$.

Figure 3a shows the z=0 cumulative GLF obtained without applying the weighting schemes: the continuous histogram uses the raw number counts; weighting galaxies by $N_{\rm Detect}/N_{\rm Field}$ results in the dotted histogram i.e. a very small correction for the faintest objects. The overplotted lines indicate the cumulative GLF obtained by Kochanek et al. (2001), normalised appropriately for each histogram. Figure 3b shows the cumulative GLF obtained after applying the two different weighting schemes: the continuous histogram uses weights according to spatial distribution and the dotted histogram according to apparent magnitude. Clearly the shape of the GLF is independent of the weighting scheme adopted for the galaxies. Again, the predicted GLF is overplotted, normalised appropriately for each histogram. The dashed line will be discussed in Section 5.4.2. The lack of any particularly large vertical displacements in any of the histograms shows that the form of the cumulative GLF is not dominated by a small number of galaxies with large weights.

There is a clear excess in the number of galaxies brighter than M^*_K, reaching a factor $\simeq$ 2 at $M_K = -23.5$ and increasing to a factor of $\simeq$ 3 at $M_K = -24.0$.

5.2 Galaxy morphologies

Given the signal-to-noise ratio of the target imaging was set in order to achieve detections of $K \simeq 20$ galaxies the quality of the images is not in general sufficient to provide much quantitative information on the morphologies of the galaxies. Visual inspection of Fig. 1 and the SEXTRACTOR-ellipticities indicate the presence of a proportion of elongated images, suggesting that at least some of the galaxies possess luminous disk components. There are certainly examples of high surface brightness galaxies with substantial bulge components (e.g. SDSS J132323.78-002155.2, SDSS J173559.95+573105.9) and overall the K-band images provide no strong evidence for a distribution of morphological properties that differ from those evident for the general population of $\sim M^*$ galaxies at $z{\sim}1$ in imaging surveys.

A link between Ca II absorbers and interacting systems has been suggested (Bowen 1991). Without redshifts to establish which of the galaxies among the seven absorbers with more than one galaxy within 6.″0 are associated with the absorbers, it is difficult to perform a strong test for an excess of close pairs.

5.3 The projected separation of the absorbers and the associated galaxies

The angular separations of the centers of the galaxies from the absorbers are given in Col. 4 of Table 2. By assuming each galaxy is at the associated absorber redshift and converting the angular separations into kpc, we can calculate the typical impact parameters. Again, the galaxies are weighted using the two different weighting schemes discussed above. The median projected distance using separation- and magnitude-based weighting is 22.7 kpc and 25.3 kpc respectively, with the value for the weighting based on separation smaller as expected. However, the relatively small systematic difference gives confidence in the results and we adopt a value of 24±2 kpc for the median projected separation between the Ca II absorbers and the associated galaxies.

With chance projections constituting a third of the galaxy images within 6.″0 of the absorbers extracting quantitative information concerning the relationship between galaxy luminosity, impact parameter and absorber properties is not really viable. Inspection of the distribution of such parameters do not reveal any convincing trends but definitive conclusions must await the acquisition of redshifts for the galaxies.

5.4 The missing galaxies

The statistical excess of galaxies about the Ca II absorber quasars establishes an association between the Ca II absorbers and the observed galaxies but for approximately a third of the absorbers no associated galaxy is seen. Potential explanations for the nature of the 'missing' galaxies fall into two categories. In the first, a residual concern for all imaging surveys of quasar absorber fields, *all* the galaxies directly responsible for the absorbers are in fact faint dwarf or low surface brightness galaxies, and the bright galaxies we observe are simply neighbours associated through clustering. In the second category, the missing galaxies form part of the same galaxy population as those producing the statistical excess, but limitations imposed by the sensitivity of the observations result in the non–detections of the fainter or more–distant galaxies. We look at each option in turn.

5.4.1 All absorber galaxies are undetected dwarf galaxies

Could the galaxies directly associated with the absorbers *all* be faint ($M_K \gtrsim M^*_K + 1.5$), likely possess small impact parameters, and thus remain undetected for all the absorbers? In such a model the observed excess of luminous galaxies within 6.″0 arises from the strong spatial clustering of galaxies on $\lesssim$50 kpc scales. An obvious example to illustrate this hypothesis is the Local Group, in which absorber sightlines passing through the Magellanic clouds would be associated from afar with the Milky Way or Andromeda. Indeed similar scenarios have often been invoked to explain the low metallicities and dust contents of DLAs.

Observationally, the determination of the clustering amplitude of dwarf galaxies close to $\sim M^*$-galaxies is difficult and the constraints remain uncertain (e.g. Lake & Tremaine 1980; van den Bosch et al. 2005; Chen et al. 2006). At $z \sim 1$, local results may not apply in anycase. Theoretically, Cold Dark Matter simulations continue to overpredict the number of satellite galaxies (Diemand, Moore, & Stadel 2004), but additional processes may be important in determining the frequency of satellites (e.g. Moore et al. 2006).

We will return to this scenario in the discussion of the true nature of the Ca II absorbers, suggesting the type of observations required to definitively confirm it or otherwise.

Table 4. K-corrections and absolute magnitudes ($H_0 = 100\,\mathrm{km\,s^{-1}}$) for K_{MKO}-band observations of Coleman, Wu, & Weedman (1980) E- and Scd-template galaxy spectra as extended by Bolzonella, Miralles, & Pelló (2000). The absolute magnitudes are calculated using the average of the E and Scd K-corrections at each redshift.

z	E K-correction	Scd K-correction	$K = 18.0$			$K = 20.0$		
			$M_K(z=0)$	$M_K(z)$	$L_K(z)/L_K^*(z)$	$M_K(z=0)$	$M_K(z)$	$L_K(z)/L_K^*(z)$
0.60	-0.598	-0.680	-23.32	-23.64	0.93	-21.32	-21.64	0.15
0.70	-0.641	-0.727	-23.69	-24.06	1.31	-21.69	-22.06	0.21
0.80	-0.678	-0.771	-24.00	-24.42	1.74	-22.00	-22.42	0.28
0.90	-0.707	-0.810	-24.28	-24.76	2.25	-22.28	-22.76	0.36
1.00	-0.739	-0.851	-24.53	-25.06	2.83	-22.53	-23.06	0.45
1.10	-0.757	-0.884	-24.76	-25.34	3.50	-22.76	-23.34	0.55
1.20	-0.752	-0.908	-24.99	-25.63	4.33	-22.99	-23.63	0.69
1.30	-0.736	-0.923	-25.20	-25.89	5.25	-23.20	-23.89	0.83
1.40	-0.699	-0.932	-25.41	-26.15	6.37	-23.41	-24.15	1.01
1.50	-0.669	-0.944	-25.61	-26.41	7.66	-23.61	-24.41	1.21
1.60	-0.635	-0.954	-25.79	-26.64	9.04	-23.79	-24.64	1.43
1.70	-0.603	-0.962	-25.97	-26.87	10.67	-23.97	-24.87	1.69
1.80	-0.584	-0.967	-26.13	-27.08	12.36	-24.13	-25.08	1.96
1.90	-0.564	-0.971	-26.28	-27.29	14.19	-24.28	-25.29	2.25
2.00	-0.550	-0.974	-26.42	-27.48	16.14	-24.42	-25.48	2.56

5.4.2 *Only a fraction of absorber galaxies remain undetected*

There are three options for hiding the remaining third of the galaxies that are unobserved: (i) they lie at more than 6.″0 from the absorber; (ii) they are hidden by the PSF of the background quasar; or (iii) they are fainter than the survey limit. Here we discuss each scheme, to determine whether any option allows the unobserved galaxies to form part of the same galaxy population that we do observe.

(i) They are distant from the absorber. The finite size of our sample means that sensitivity to the presence of excess galaxies at separations beyond ∼50 kpc is limited. However, the statistics of the galaxy surface density in the annulus 6.″0-12.″0 (≃50-100 kpc) surrounding the Ca II absorbers show no evidence for any excess (Table 5, Figure 2), with observed:predicted numbers of 11:12.5 ($K \leqslant 19.0$) and 28:28.8 ($K \leqslant 20.0$). Although a small number of galaxies may indeed fall outside of the 6.″0 annulus, it is not possible to explain the majority of the missing galaxies in this way.

(ii) They are hidden by the quasar PSF. As discussed in Section 3.3, the detectability of even relatively bright, $K \simeq 19.0$, galaxies declines rapidly at very small separations, $\Delta\theta \lesssim 0.''25$ and the possibility that a substantial fraction of the absorbers occur within impact parameters of $\lesssim$3 kpc of the centers of intermediate luminosity galaxies cannot be ruled out directly. However, the distribution of projected absorber-galaxy separations for $\Delta\theta \geqslant 0.''5$ shows no evidence for a rapid increase in the frequency of galaxies at very small impact parameters. A single population drawn from the same $(\Delta\theta, M_K)$ distribution as observed is thus ruled out, although a discontinuity in the distribution of absorber–galaxy separations is allowed by the observations.

(iii) They are faint. Perhaps the missing galaxies possess a similar distribution of absorber-galaxy separations but have magnitudes fainter than the $\simeq M_K^* + 1.5$ limit of the K-band images? Previous studies of the absorption cross–sections of galaxies (e.g. Steidel, Dickinson, & Persson 1994), have found a luminosity dependence of the observed size of absorbing regions associated with galaxies of the form,

$$\sigma(L) = \sigma^* \left(\frac{L}{L^*}\right)^\beta \tag{3}$$

where σ^* is the cross-section for an L^* galaxy. Adopting such a luminosity dependent scaling for the Ca II absorbers, with $\beta = 0.7$, produces an excellent fit to the galaxy luminosity function for the galaxies brighter than the $\simeq M^* + 1.5$ limit of our observations (Fig. 3). Given the shallow slope, $\alpha = -1.09$, of the Kochanek et al. (2001) GLF, combined with the strong bias towards luminous galaxies, the integrated cross–section of the galaxy population converges rapidly at faint magnitudes. Adopting a faint limit of $M^* + 5$ for the integration results in a prediction that ≃60 per cent of the absorber cross–section should result from galaxies brighter than our observational limit of $M^* + 1.5$, in good agreement with the fraction of our 30 absorbers where we see such a galaxy. Given the power law luminosity–dependent scaling provides an effective and simple parameterisation of our results, we adopt the relation in order to make quantitative estimates of the filling-factor of the Ca II absorption and to compare the properties of the Ca II absorbers with other classes of quasar absorption systems.

6 DISCUSSION

6.1 The Ca II absorbers and their associated galaxies

The K-band imaging results of the Ca II systems provide new constraints on the relationship between Ca II absorbers and their associated galaxies. In Wild, Hewett, & Pettini (2007, Section 4.1) we used observations of DLAs, together with the relative number densities of DLAs and Ca II absorbers, to propose that Ca II absorption can arise at projected radii of ∼ 10 kpc from the centre of a galaxy. This simple calculation assumes a circular geometry for the absorbers and a unit filling factor (i.e. the gas is not patchy). Clearly, this model contrasts with the much larger value of 24 kpc derived from the K-band imaging. Our imaging results reveal that the dominant contributor to the Ca II cross-section is *not* the inner part of more extended DLA absorbers, centred on relatively luminous galaxies. Rather, the Ca II absorbers themselves trace much larger structures associated primarily with luminous galaxies where the filling factor is low.

Taking the value of $dP/dz = 0.025$ from Wild, Hewett, & Pettini (2007) for Ca II absorbers at $z \simeq 1$ and integrating the luminosity-dependent absorber cross–section

Table 6. Absorber properties: rest-frame equivalent widths (W) of Ca II , Mg II , Mg I and Fe II absorption lines and errors. The final column gives neutral Hydrogen column densities from Rao, Turnshek, & Nestor (2006).

Name	z_{abs}	$W_{\lambda 3935,3970}$	err	$W_{\lambda 2796,2803}$	err	$W_{\lambda 2853}$	err	$W_{\lambda 2600}$	err	N(HI)
J074804.06+434138.5	0.898	0.62,0.53	0.23,0.16	1.69,1.17	0.12,0.08	0.30	0.13	0.68	0.16	—
J080735.97+304743.8	0.969	0.65,0.77	0.16,0.14	2.51,2.40	0.13,0.09	1.21	0.14	2.15	0.15	—
J081930.35+480825.8	0.903	0.68,0.34	0.12,0.07	1.66,1.53	0.08,0.05	1.00	0.10	1.39	0.10	—
J083819.85+073915.1	1.133	0.71,1.15	0.26,0.41	2.63,2.42	0.13,0.09	0.67	0.16	1.70	0.15	—
J085221.25+563957.6	0.844	0.66,0.49	0.22,0.18	3.29,3.02	0.16,0.11	1.18	0.23	2.52	0.18	—
J085556.63+383232.7	0.852	0.46,0.07	0.13,0.07	2.68,2.53	0.09,0.06	0.70	0.13	2.30	0.10	—
J093738.04+562838.8	0.978	1.23,0.53	0.28,0.19	4.88,4.27	0.25,0.20	2.42	0.31	3.51	0.30	—
J095307.05+111140.8	0.980	0.88,0.69	0.30,0.25	2.34,2.33	0.21,0.15	1.84	0.33	2.05	0.32	—
J095352.69+080103.6	1.023	0.48,0.35	0.13,0.09	0.85,0.76	0.07,0.05	0.40	0.21	0.58	0.08	—
J100339.44+101936.8	0.816	0.76,0.57	0.23,0.15	1.46,1.31	0.15,0.11	0.55	0.19	1.35	0.17	—
J105930.50+120532.8	1.050	1.85,0.66	0.39,0.17	1.71,1.97	0.24,0.18	0.94	0.39	2.11	0.26	—
J110729.03+004811.2	0.740	0.41,0.22	0.06,0.04	2.89,2.79	0.04,0.02	0.85	0.05	2.33	0.04	$21.00^{+0.02}_{-0.05}$
J113357.55+510844.9	1.029	1.16,0.58	0.40,0.24	2.65,2.73	0.21,0.17	0.75	0.29	1.94	0.23	—
J115523.97+480141.6	1.114	2.21,1.45	0.70,0.49	3.67,3.15	0.36,0.26	1.33	0.30	3.84	0.45	—
J120300.96+063440.8	0.862	1.34,1.05	0.28,0.19	5.65,5.04	0.35,0.27	3.03	0.49	3.77	0.53	—
J122144.62-001141.8	0.929	0.59,0.29	0.18,0.11	0.99,0.84	0.13,0.09	0.75	0.20	0.71	0.15	—
J122756.35+425632.4	1.045	0.34,0.17	0.10,0.06	1.58,1.37	0.07,0.05	0.25	0.12	1.14	0.07	—
J124659.81+030307.6	0.939	0.95,0.58	0.36,0.16	2.92,2.80	0.19,0.14	1.28	0.22	2.13	0.26	—
J130841.19+133130.5	0.951	0.73,0.70	0.26,0.20	1.82,1.63	0.18,0.13	0.73	0.20	1.09	0.22	—
J132323.78-002155.2	0.716	0.95,0.55	0.10,0.07	2.16,1.98	0.11,0.07	0.97	0.13	1.44	0.13	$20.54^{+0.15}_{-0.15}$
J132346.05-001819.8	1.087	1.07,0.54	0.37,0.38	4.24,4.06	0.53,0.40	2.00	0.63	2.98	0.36	—
J140444.19+551636.9	1.070	0.94,0.50	0.36,0.22	1.96,1.83	0.26,0.19	0.68	0.25	1.42	0.23	—
J145633.08+544831.6	0.879	0.42,0.40	0.16,0.10	4.01,3.72	0.12,0.08	1.66	0.19	3.09	0.15	—
J151247.48+573843.4	1.044	1.00,0.53	0.26,0.16	2.02,2.27	0.20,0.14	0.73	0.38	1.59	0.23	—
J153503.36+311832.4	0.904	0.77,0.26	0.15,0.10	2.16,1.86	0.12,0.09	0.77	0.16	0.98	0.12	—
J155529.40+493154.9	0.893	0.38,0.18	0.12,0.07	2.25,2.06	0.08,0.06	0.71	0.09	1.53	0.11	—
J160932.95+462613.3	0.966	0.75,0.28	0.28,0.16	1.01,0.86	0.15,0.10	0.52	0.35	0.69	0.16	—
J164350.94+253208.8	0.885	0.54,0.13	0.20,0.13	0.85,0.65	0.09,0.06	0.19	0.08	0.45	0.09	—
J172739.01+530229.2	0.945	0.62,0.61	0.15,0.12	2.69,2.56	0.10,0.07	0.99	0.13	2.23	0.12	$21.16^{+0.04}_{-0.05}$
J173559.95+573105.9	0.872	0.80,0.68	0.18,0.12	1.98,1.76	0.12,0.08	0.83	0.15	1.53	0.16	—

Table 5. Companion galaxy surface number densities in the 30 absorber and five control fields, as a function of separation from the quasar. Counts for galaxies with $K \leqslant 20$ and $K \leqslant 19$ are both given.

Separation (")	Observed Absorbers	Predicted	Observed Controls	Predicted
(a) $K \leqslant 20.0$				
$\leqslant$1.0	3	0.3	1	<0.1
$\leqslant$2.0	9	1.1	1	0.2
$\leqslant$3.0	14	2.4	1	0.4
$\leqslant$4.0	18	4.3	1	0.7
$\leqslant$5.0	23	6.7	1	1.1
$\leqslant$6.0	30	9.6	1	1.6
6.0–12.0	28	28.8	5	4.8
(b) $K \leqslant 19.0$				
$\leqslant$1.0	2	0.1	1	<0.1
$\leqslant$2.0	6	0.5	1	0.1
$\leqslant$3.0	10	1.0	1	0.2
$\leqslant$4.0	11	1.9	1	0.3
$\leqslant$5.0	11	2.9	1	0.5
$\leqslant$6.0	16	4.2	1	0.7
6.0–12.0	11	12.5	2	2.1

(Section 5.4.2) using the Kochanek et al. (2001) GLF down to $M^* + 5$ produces a value of $\sigma^* = 400\,\mathrm{kpc}^2$, equivalent to a radius, $R^* = 11.4\,$kpc. Our observations produce an observed mean galaxy-absorber separation of 24 kpc for galaxies with $M = M^*$, leading to a maximum radius out to which an absorber may be detected[4] of 36 kpc. The inferred filling-factor is thus only $(11.4/36)^2$=0.1.

The large mean projected separations observed also provide an explanation for the small contribution of the Ca II absorbers to the star formation rate density at $z \sim 1$ determined by Wild, Hewett, & Pettini (2007) from [O II] $\lambda\lambda$3727,3730 emission observed in the SDSS spectra. The fraction of the K-band luminosity of the associated galaxies that would fall within the 3$''$.0 diameter of the SDSS spectroscopic fibres is only 30$\pm$5 per cent. Thus, the star formation associated with the central luminous parts of the associated galaxies would have been missed and, assuming the observed galaxies are directly responsible for the absorption, the results of Wild, Hewett, & Pettini (2007) do not constrain directly the contribution of Ca II absorber galaxies to the star formation rate of the Universe at $z \sim 1$.

6.2 Comparison with results for other absorber classes

In this section we compare our imaging results to those for the more familiar classes of strong Mg II absorbers and DLAs.

[4] The mean observed impact parameter is about two-thirds of the maximum radius, assuming the absorbers present simple circular cross-sections.

6.2.1 Mg II *absorbers*

The Mg II equivalent widths of the Ca II absorbers are very large; the mean rest-frame Mg II $W_{\lambda 2796}$ of the sample imaged in this paper is 2.44 Å, with a minimum value of 0.85 Å, and 18 of the 30 systems have equivalent widths greater than 2.0 Å (Table 6). Where possible, we therefore focus on results for similarly strong Mg II absorbers.

The only published galaxy luminosity function for Mg II absorbers is from the survey of 52 absorbers by Steidel, Dickinson, & Persson (1994), who find that, after correcting for an observed dependence of gas cross-section on galaxy luminosity ($\sigma \propto L^{0.4}$), the K-band luminosity function of Mg II absorbers in the redshift range $0.2 \leqslant z \leqslant 1.0$ is consistent with the z=0 luminosity function of Mobasher, Sharples, & Ellis (1993). This implies a weaker galaxy luminosity-dependence of the cross-section than for Ca II absorbers. Several caveats apply to the comparison with Steidel et al.'s result. Firstly, the Mg II equivalent width distribution of the absorber sample differs considerable from ours, with their systems selected to have $W_{\lambda 2796}$ >0.3 Å. Secondly, a recent reassessment of the identification procedure for host galaxies in this survey by Churchill, Steidel, & Kacprzak (2005), has revealed a small number of potential systematic biases which remain to be investigated.

Our second comparison is with the r-band imaging of the environments of 15 very strong, $W_{\lambda 2796} \geqslant 2.7$ Å, Mg II absorbers with redshifts $0.42 < z < 0.84$ by Nestor et al. (2006). The principal result is the detection, in essentially all cases, of a galaxy, which, if physically associated with the absorber, lies projected within 40 kpc of the quasar and has luminosity $L \gtrsim 0.3L^*$. Seven of the sample are Ca II absorbers, and six of these possess a galaxy within 40 kpc with luminosities $0.3L^* \lesssim L \lesssim 2.0L^*$. Allowing for the chance projection of one or two galaxies, the results are entirely consistent with the findings presented in this paper.

The second result of the Nestor et al. study is the detection of an excess of apparently bright galaxies, which, if physically associated with the absorber, have projected separations extending to ∼150 kpc and extremely high luminosities, $4L^* \lesssim L \lesssim 13L^*$. We can perform a similar analysis using our dataset by comparing the observed number of galaxies brighter than $4L^*_K(z)$ if placed at z_{abs} in each of our Ca II absorber field images (which extend to ≃150 kpc from the quasars) to the predictions from the K20-survey number-magnitude distribution. Eight field galaxies are predicted, whereas we find a total of 11 such galaxies around eight quasars. Thus, we find no evidence in our sample for any such excess. Nestor et al. discuss an interpretation for the observed excess in terms of elevated levels of star-formation in the galaxies. At the rest-frame wavelengths of ∼4000 Å probed by their observations, they are certainly far more affected by the presence of ongoing and recent star-formation than the ∼10 000 Å wavelengths probed by our K-band observations. However, we note that the `PhotoZ` photometric redshifts from the SDSS DR5 (Adelman-McCarthy et al. 2007) for all of their galaxies with $L \geqslant 4L^*$ are consistent with their lying at considerably lower redshifts than the absorbers, supporting their identification as more typical objects at lower redshifts[5].

Finally, a powerful constraint on the luminosities of galaxies associated with Mg II absorbers comes from the stacking analysis of SDSS images in the regions around Mg II absorbers by Zibetti et al. (2006). The mean integrated rest-frame luminosity within 100 kpc of their sample of Mg II absorbers with redshifts $0.76 \leqslant z \leqslant 1.0$ is $M_i(z) = -22.4$ (AB system). The absolute magnitude corresponds to $\simeq M^* - 0.5$, or $M^*(z$=0). At lower redshifts, where the signal is strong enough for division of the sample, Zibetti et al. (2006) find only a small difference between the mean absolute magnitudes of galaxies associated with all the Mg II absorbers and those associated with the strongest absorbers. Assuming the same holds for the $0.76 \leqslant z \leqslant 1.0$ absorber sample, and noting that approximately half the luminosity within 100 kpc lies within the smaller aperture of 50 kpc, produces an average absolute magnitude of $\simeq M^*(z$=0)+0.75. The 50 kpc aperture corresponds closely to the spatial scale of our observed excess of galaxies and the average absolute magnitude of galaxies associated with all 30 Ca II absorbers is $\simeq M^*(z$=0)+0.25±0.2. The estimate is insensitive to whether the galaxies associated with the nine absorbers without detected galaxies are excluded or included (even assuming detections at the K=20.0 limit). The somewhat brighter mean galaxy luminosity associated with the Ca II absorbers is consistent with the stronger galaxy luminosity-dependence of the cross-section ($\sigma \propto L^{0.7}$) compared to that for Mg II absorbers ($\sigma \propto L^{0.4}$).

6.2.2 DLA absorbers

Notwithstanding recent efforts (Rao, Turnshek, & Nestor 2006), the number of known DLA-systems at redshifts $z \lesssim 1$, where imaging studies of host galaxies are most effective, is small. Chen, Kennicutt, & Rauch (2005) provide a summary of relevant imaging studies and four additional systems have been imaged by Chun et al. (2006). Follow-up studies of a small number of the galaxies associated with the DLAs have also been undertaken (e.g. Chen et al. 2005; Gharanfoli et al. 2007). Even from the limited statistics available it is clear that the galaxies associated with DLAs exhibit an extended range in the distributions of both luminosity and impact parameter. Our results for the three confirmed DLAs (Table 6) reinforce the conclusion, with one non-detection, one luminous galaxy with a small (8 kpc) impact parameter and one intermediate luminosity galaxy with a significant (30 kpc) impact parameter. The statistics are as yet too poor to allow strong conclusions to be drawn but the observed distribution of luminosity and impact parameter for the galaxies associated with the Ca II absorbers is consistent with what is known for DLAs.

7 CONCLUDING REMARKS

As discussed in Section 1, the nature of quasar absorption line systems is still a matter of considerable debate. The Steidel et al. (1994) model of Mg II absorbers with $W_{\lambda 2796} > 0.3$ Å residing within spherical halos of radius ≃40 kpc and unity filling factor has strongly influenced our picture of quasar absorption line systems for the past decade. However, alternative models have been suggested (e.g. Charlton & Churchill 1996) and recent imaging results indicate that substantially larger impact parameters are common and filling factors less than unity are necessary (Churchill, Kacprzak, & Steidel 2005; Zibetti et al. 2006).

Theories range from identifying absorption systems with: extended disks, large gaseous haloes, outflows from superwinds, or, extended debris from mergers/interactions. Although models are currently not well advanced, determining the relation between absorption line systems (with different metal line and dust properties) and the properties of their hosts (impact parameters, luminosity and

[5] Such an interpretation does not explain why such an excess of galaxies at redshifts $z_{gal} << z_{abs}$ is observed

morphologies), should lead to a better understanding of the origins of absorption line systems and their relevance to galaxy evolution.

In Wild et al. (2006) we found the dust content of Ca II absorption line systems to differ from those of Mg II absorption line systems in the same redshift range and with the same Fe II and Mg II equivalent width properties. More specifically, the Ca II absorption line systems have $E(B-V)$ = 0.06 compared to 0.008 for the entire Mg II /Fe II selected sample, or 0.02 for the 30 per cent with the strongest absorption lines. After correcting for dust obscuration bias, the distribution of dust contents in the Ca II absorbers starts to approach that seen in emission-selected galaxies at similar redshifts, a very different story to that seen in DLAs. Without N(H I) measures it is difficult to place constraints on their absolute metallicities, however, their dust-to-metals ratio similar to that found in the Milky Way suggests a high degree of chemical enrichment. To summarise, the absorption properties of the Ca II absorbers point strongly towards them tracing dense, metal and dust rich gaseous clouds. The number densities of Ca II absorbers, after correcting for dust obscuration bias, is ∼30 per cent that of DLAs at similar redshifts and a plausible scenario was that, while DLAs could be found out to extended radii from the center of galaxies, Ca II absorbers traced the innermost, star-forming, disks.

In Wild et al. (2007) we showed that the average star formation within 1.″5–radii of strong Ca II absorbers is four times that associated with strong Mg II absorbers. However, if it is assumed that the Ca II absorbers surround galaxies with close to unit filling factor, the galaxies responsible for Ca II absorption only account for ∼3 per cent of the observed global star formation[6].

The results of the present paper reveal a very different picture for the nature of the Ca II absorber hosts. We find there is a very strong bias towards selecting luminous galaxies, and the Ca II absorbing clouds are found out to large physical distances from these luminous galaxies. Our observations provide an explanation for the low measured *in situ* star formation rate within 1.″5 ($\lesssim$10 kpc) of the Ca II absorbers measured by Wild et al. (2007). However, the origin of high column density, dusty, chemically enriched gas clouds at up to 50 kpc from luminous galaxies remains unclear. There are several competing theories and further observations are required to discriminate between the models.

- Given the observed bias of our sample towards bright galaxies, a possible explanation is that the Ca II absorbers lie within extended gaseous disks such as those being discovered with the GALEX satellite (Thilker et al. 2005). These ultraviolet–bright disks are found to coincide with neutral hydrogen structures, in which dust-to-gas ratios as high as the central regions of the galaxy are found (Popescu & Tuffs 2003), in apparent agreement with the relatively high dust contents of the Ca II absorbers.
- Possibly, the true absorber hosts are dwarf galaxies, associated, through spatial clustering, with the larger galaxies seen in the K-band images. Within the Local Group, the LMC and SMC lie at ∼50 and 60 kpc from the Milky Way, and while more than half of the MW satellites lie within 50 kpc, none contain significant quantities of gas (Belokurov et al. 2007). A similar distribution of satellites is seen for M31 (McConnachie & Irwin 2006). Outside of our immediate neighbourhood, Zaritsky et al. (1993) find on average less than 1.5 satellites[7] within 500 kpc of local spiral galaxies. Although the picture may be very different at $z \sim 1$, the 10 per cent covering factor for Ca II absorption derived in the present paper currently makes this scenario seem unlikely. High resolution ultraviolet, or possibly Hα, imaging (for example with the Hubble Space Telescope) would reveal the existence of compact regions of star formation close to the absorber, such as seen in the LMC, and distinguish between an origin for the absorbers in the form of an extended disk associated with the luminous galaxies or from discrete dwarf galaxies.
- Perhaps Ca II absorbers are the relics of outflows from previous episodes of intense star formation in the luminous galaxies, but it is not clear how dense clouds would survive the ∼10^8 yr to reach such distances at typical starburst outflow speeds without being dispersed and the dust grains destroyed. Ca II is regularly detected in local High and Intermediate Velocity Clouds (HVCs and IVCs), potential candidates for such outflow relics from the Milky Way. However, none are found to have Ca II column densities approaching 1.7×10^{12} to $1.3 \times 10^{13}\mathrm{cm}^{-2}$ as seen in our systems (Wakker 2001; Thom et al. 2006) (although this may simply reflect lower Hydrogen column densities of the clouds). High-resolution imaging and spectroscopy of the galaxies could indicate the likelihood of such a scenario by measuring the relative angle of the major axis of the galaxy to the absorber and determining the recent star formation history of the galaxies.
- Finally, within standard galaxy evolution scenarios, tidal debris from cannibalism of small galaxies by larger galaxies is expected to fill a much greater volume around galaxies at z∼1 than around galaxies today. In the local Universe, the SDSS has had a large impact on the detection of tidal streams around the Milky Way. Such streams cover hundreds of square degrees on the sky and lie at several tens of kpcs from the center of the Milky Way (Ibata et al. 1997; Yanny et al. 2003; Belokurov et al. 2006). Similarly to HVCs, the H I column densities of the streams tend to be lower than the DLA limit of 3×10^{20}: mean columns in the Magellanic Stream are of order 4×10^{18} to 4×10^{19} (Putman et al. 2003)[8]. Ca II has been observed in absorption in the Magellanic Bridge, but again with much lower column densities than found in our high redshift Ca II absorbers (Smoker et al. 2005). Perhaps, a better local comparison might be with the M81 group, in which a complex filamentary structure of high column density neutral Hydrogen tails appear to have been caused by the interaction between M81 and two neighbouring galaxies (Yun, Ho, & Lo 1994). NGC 5291 (Boquien et al. 2007) is another example of a system where significant columns of gas and associated star formation extend over large regions surrounding prominent galaxies.

The high equivalent width Ca II absorption systems that comprise our sample are extremely rare in the local Universe but an understanding of the origins of the few that do exist may reveal the physical mechanism responsible for strong Ca II absorption. Spectroscopy of a small number of luminous galaxies associated with low-redshift Ca II absorbers has been undertaken by Zych et al. (2007). The galaxies, predominantly spirals, possess high metallicities and exhibit substantial star formation rates. Further progress with such investigations would greatly aid in our interpretation of results at higher redshift.

[6] Modest corrections to obtain the true star formation rate due to extinction by dust may be appropriate.
[7] Satellites were defined as objects 2.2 mag fainter than the primary galaxy; most detected satellites were found to be 2.2 to 6 magnitudes fainter than the primary.
[8] The resolution of these measurements is 15.5 arcmins.

ACKNOWLEDGMENTS

We would like to thank Emma Ryan-Weber, Chris Thom, Martin Zwaan and Alan McConnachie for valuable discussions, and the anonymous referee for useful comments. VW is supported by the MAGPOP Marie Curie EU Research and Training Network. The United Kingdom Infrared Telescope is operated by the Joint Astronomy Centre on behalf of the U.K. Particle Physics and Astronomy Research Council. An anonymous referee provided a careful reading of the original manuscript that resulted in a number of improvements to the paper.

Funding for the Sloan Digital Sky Survey (SDSS) has been provided by the Alfred P. Sloan Foundation, the Participating Institutions, the National Aeronautics and Space Administration, the National Science Foundation, the U.S. Department of Energy, the Japanese Monbukagakusho, and the Max Planck Society. The SDSS Web site is http://www.sdss.org/. The SDSS is managed by the Astrophysical Research Consortium (ARC) for the Participating Institutions. The Participating Institutions are The University of Chicago, Fermilab, the Institute for Advanced Study, the Japan Participation Group, The Johns Hopkins University, Los Alamos National Laboratory, the Max-Planck-Institute for Astronomy (MPIA), the Max-Planck-Institute for Astrophysics (MPA), New Mexico State University, University of Pittsburgh, Princeton University, the United States Naval Observatory, and the University of Washington.

References

Belokurov V., et al., 2006, ApJ, 642, L137
Belokurov V., et al., 2007, ApJ, 658, 337
Bertin E., Arnouts S., 1996, A&AS, 117, 393
Bolzonella M., Miralles J.-M., Pelló R., 2000, A&A, 363, 476
Boquien M., Duc P. -., Braine J., Brinks E., Lisenfeld U., Charmandaris V., 2007, A&A, in press astro, arXiv:astro-ph/0703002
Bond N. A., Churchill C. W., Charlton J. C., Vogt S. S., 2001, ApJ, 562, 641
Bowen D. V., 1991, MNRAS, 251, 649
Charlton J. C., Churchill C. W., 1996, ApJ, 465, 631
Chen H.-W., Kennicutt R. C., Jr., Rauch M., 2005, ApJ, 620, 703
Chen J., Kravtsov A. V., Prada F., Sheldon E. S., Klypin A. A., Blanton M. R., Brinkmann J., Thakar A. R., 2006, ApJ, 647, 86
Chen H.-W., Lanzetta K. M., 2003, ApJ, 597, 706
Chun M. R., Gharanfoli S., Kulkarni V. P., Takamiya M., 2006, AJ, 131, 686
Churchill C. W., Kacprzak G. G., Steidel C. C., 2005, pgqa.conf, 24
Churchill C., Steidel C., Kacprzak G., 2005, ASPC, 331, 387
Cimatti A., et al., 2002, A&A, 391, L1
Cimatti A., et al., 2002, A&A, 392, 395
Cole S., et al., 2001, MNRAS, 326, 255
Coleman G. D., Wu C.-C., Weedman D. W., 1980, ApJS, 43, 393
Diemand J., Moore B., Stadel J., 2004, MNRAS, 352, 535
Drory N., Bender R., Feulner G., Hopp U., Maraston C., Snigula J., Hill G. J., 2003, ApJ, 595, 698
Falomo R., Kotilainen J. K., Pagani C., Scarpa R., Treves A., 2004, ApJ, 604, 495
Gharanfoli S., Kulkarni V. P., Chun M. R., Takamiya M., 2007, AJ, 133, 130
Hewett P. C., Warren S. J., Leggett S. K., Hodgkin S. T., 2006, MNRAS, 367, 454
Hunter I., Smoker J. V., Keenan F. P., Ledoux C., Jehin E., Cabanac R., Melo C., Bagnulo S., 2006, MNRAS, 367, 1478
Ibata R. A., Wyse R. F. G., Gilmore G., Irwin M. J., Suntzeff N. B., 1997, AJ, 113, 634
Ivezić Ž., et al., 2002, AJ, 124, 2364
Kochanek C. S., et al., 2001, ApJ, 560, 566
Kotilainen J. K., Falomo R., Treves A., Uslenghi M., 2006, NewAR, 50, 772
Lake G., Tremaine S., 1980, ApJ, 238, L13
McConnachie A. W., Irwin M. J., 2006, MNRAS, 365, 1263
Mobasher B., Sharples R. M., Ellis R. S., 1993, MNRAS, 263, 560
Moore B., Diemand J., Madau P., Zemp M., Stadel J., 2006, MNRAS, 368, 563
Murphy M. T., Liske J., 2004, MNRAS, 354, L31
Nestor D. B., Turnshek D. A., Rao S. M., Quider A. M., 2006, astro, arXiv:astro-ph/0610760
Popescu C. C., Tuffs R. J., 2003, A&A, 410, L21
Pozzetti L., Bruzual A. G., Zamorani G., 1996, MNRAS, 281, 953
Pozzetti L., et al., 2003, A&A, 402, 837
Putman M. E., Staveley-Smith L., Freeman K. C., Gibson B. K., Barnes D. G., 2003, ApJ, 586, 170
Nestor D. B., Turnshek D. A., Rao S. M., 2005, ApJ, 628, 6
Rao S. M., Turnshek D. A., Nestor D. B., 2006, ApJ, 636, 610
Roche P. F., et al., 2003, SPIE, 4841, 901
Saracco P., et al., 2006, MNRAS, 367, 349
Schneider D. P., et al., 2005, AJ, 130, 367
Smoker J. V., Keenan F. P., Thompson H. M. A., Brüns C., Muller E., Lehner N., Lee J.-K., Hunter I., 2005, A&A, 443, 525
Steidel C. C., Dickinson M., Persson S. E., 1994, ApJ, 437, L75
Stetson P. B., 1987, PASP, 99, 191
Thilker D. A., Bianchi L., Boissier S., et al. 2005, ApJL, 619, L79
Thom C., Putman M. E., Gibson B. K., Christlieb N., Flynn C., Beers T. C., Wilhelm R., Lee Y. S., 2006, ApJ, 638, L97
van den Bosch F. C., Yang X., Mo H. J., Norberg P., 2005, MNRAS, 356, 1233
Wakker B. P., 2001, ApJS, 136, 463
Wang T. G., Dong X. B., Zhou H. Y. & Wang J. X., 2005, ApJL, 622, L101
Wild V., Hewett P. C., 2005b, MNRAS, 361, L30
Wild V., Hewett P. C., Pettini M., 2006, MNRAS, 367, 211
Wild V., Hewett P. C., Pettini M., 2007, MNRAS, 374, 292
Wolfe A. M., Gawiser E., Prochaska J. X., 2005, ARA&A, 43, 861
Yanny B., et al., 2003, ApJ, 588, 824
York D. G., et al., 2006, MNRAS, 367, 945
Yun M. S., Ho P. T. P., Lo K. Y., 1994, Nature, 372, 530
Zaritsky D., Smith R., Frenk C., White S. D. M., 1993, ApJ, 405, 464
Zibetti S., Menard B., Nestor D. B., Quider A. M., Rao S. M., Turnshek D. A., 2007, ApJ, in press (astro, arXiv:astro-ph/0609760)
Zych B. J., Murphy M. T., Pettini M., Hewett P. C., Ryan-Weber E. V., Ellison S. L., 2007, MNRAS, in press

APPENDIX A: NOTES ON INDIVIDUAL OBJECTS

The general discussion in Section 3.3 and the image-subtractions shown in Fig. 1 summarises the status of the subtractions for the majority of objects. However, in a small number of cases, some specific comments are warranted:

SDSS J085556.63+383232.7 (z_{abs}=0.852; z_{quasar}=2.065): the low surface brightness structure to the north-west of the quasar does not reproduce consistently when using different PSF-stars in the subtractions.

SDSS J093738.04+562838.8 (z_{abs}=0.980; z_{quasar}=1.798): the faint apparent 'donut' residual does reproduce when different PSF-stars are used. However, the residual is slightly off-centre from the quasar image and extensive interactive scaling of the PSF-stars fails to produce a convincing galaxy-like image. The quasar redshift is high, making the identification of a host galaxy as the origin of the residual unlikely but it is possible that a galaxy with a small galaxy-quasar separation, $\Delta\theta \lesssim 0\farcs3$, is present.

SDSS J105930.50+120532.8 (z_{abs}=1.050; z_{quasar}=1.570): the subtraction shown employs a rather faint PSF-star from the quasar image itself. The noise level is thus enhanced but there is no systematic flux excess above the the $K = 20.0$ detection threshold for the galaxy catalogue. PSF-stars from the library of PSF-stars confirm the lack of any extended residual but at the expense of more prominent 'cloverleaf' residuals on small scales.

SDSS J110729.03+004811.2 (z_{abs}=0.740; z_{quasar}=1.391): the subtraction shown employs a PSF derived from seven relatively faint stars in the frame. The noise level in the subtracted frame is enhanced but the SEXTRACTOR image analysis of the PSF-subtracted frame results in no object brighter than $K = 20.3$ being detected. Individual PSF stars from the PSF-library result in small-scale 'butterfly' residuals but provide no evidence for the presence of any galaxy image with $K \lesssim 20.5$

SDSS J122756.35+425632.4 (z_{abs}=1.045; z_{quasar}=1.310): the faint apparent residual approximately $0\farcs5$ to the south does not reproduce well when different PSF-stars are used.